

The Effect of Hydrogen Peroxide on Uranium Oxide Films on 316L Stainless Steel

Richard J. Wilbraham^a, Colin Boxall^{a}, David T. Goddard^b, Robin J. Taylor^c, Simon Woodbury^c*

^aThe Lloyd's Register Foundation Centre for Nuclear Engineering, Engineering Department, Lancaster University, Bailrigg, Lancashire, LA1 4YR, United Kingdom

^bNational Nuclear Laboratory, Preston Laboratory, Springfields, Preston, Lancashire, PR4 0XJ, United Kingdom

^cNational Nuclear Laboratory, B170 Central Laboratory, Seascale, Cumbria, CA20 1PG, United Kingdom

r.wilbraham@lancaster.ac.uk, c.boxall@lancaster.ac.uk, dave.t.goddard@nnl.co.uk,
robin.j.taylor@nnl.co.uk, simon.woodbury@nnl.co.uk

RECEIVED DATE

*To whom all correspondence should be sent. E-mail: c.boxall@lancaster.ac.uk. Tel.: +44 1524 593109

ABSTRACT: For the first time the effect of hydrogen peroxide on the dissolution of electrodeposited uranium oxide films on 316L stainless steel plachets (acting as simulant uranium-contaminated metal surfaces) has been studied. Analysis of the H₂O₂-mediated film dissolution processes via open circuit potentiometry, alpha counting and SEM/EDX imaging has shown that in near-neutral solutions of pH 6.1 and at [H₂O₂] ≤ 100 μmol dm⁻³ the electrodeposited uranium oxide layer is freely dissolving, the

associated rate of film dissolution being significantly increased over leaching of similar films in pH 6.1 peroxide-free water. At H_2O_2 concentrations between 1 mmol dm^{-3} and 0.1 mol dm^{-3} , formation of an insoluble studtite product layer occurs at the surface of the uranium oxide film. In analogy to corrosion processes on common metal substrates such as steel, the studtite layer effectively passivates the underlying uranium oxide layer against subsequent dissolution. Finally, at $[\text{H}_2\text{O}_2] > 0.1 \text{ mol dm}^{-3}$ the uranium oxide film, again in analogy to common corrosion processes, behaves as if in a transpassive state and begins to dissolve.

This transition from passive to transpassive behaviour in the effect of peroxide concentration on UO_2 films has not hitherto been observed or explored, either in terms of corrosion processes or otherwise. Through consideration of thermodynamic solubility product and complex formation constant data, we attribute the transition to the formation of soluble uranyl-peroxide complexes under mildly alkaline, high $[\text{H}_2\text{O}_2]$ conditions – a conclusion that has implications for the design of both acid minimal, metal ion oxidant-free decontamination strategies with low secondary waste arisings, and single step processes for spent nuclear fuel dissolution such as the Carbonate-based Oxidative Leaching (COL) process.

KEYWORDS: Studtite, Uranium Corrosion, Decontamination

1. Introduction

Radioactive contamination due to ‘plate-out’ of solids, colloids or metal ions from a solution phase onto stainless steel surfaces in plant vessels, pipes, tanks etc. is a generic problem across most of, if not all, nuclear industry sites. Surface contamination of this form is broadly classified as being of two main types: non-fixed and fixed contamination. Non-fixed contamination is loosely bound to the surface through weak electrostatic interactions and is easily removed by most physical clean up techniques. The remaining steel surface may then be only slightly contaminated but the associated contaminant may be fixed in some way, e.g. molecularly bound to the solid surface, held within difficult to remove steel oxide layers or sequestered in surface features. Such fixed contamination is commonly encountered on nuclear process steels, whereon the iron oxide, austenite and Cr/Ni spinel phases forming the passivating layer at the steel surface can trap uranyl ions, initially in the +6 oxidation state, through coprecipitation as uranium iron/chromium hydroxide complexes or polymeric uranium oxyhydroxide [1-3]. During this coprecipitation, some trapped U(VI)/Fe complexes may also be reduced by ferrous ions to the tetravalent state [1,4]. Thus, the resultant contaminant layer may be considered to be a fixed mixed oxide of uranium.

For removal of these fixed uranium oxide contaminant layers, chemical and/or electrochemical decontamination techniques must be applied. Common chemical techniques are mostly redox chemistry based and involve either simple one step treatments such as the cerium oxidant based MEDOC process (Metal Decontamination by Oxidation with Cerium) [5-10] or more complex multistep processes such as the permanganate oxidant based CORD process (Chemical Oxidising Reduction Decontamination) [11-15]. Importantly, in combination with actinide/transition metal complexants such as hydroxycarboxylic acids [2] or carbonates in the COL process (Carbonate-based Oxidative Leaching) [16-19], application of hydrogen peroxide has proved to be a useful single step process for spent uranium dioxide fuel pellet dissolution. This suggests that H_2O_2 could also be used as a decontamination agent for fixed uranium oxide based contaminants. Such use of H_2O_2 would be particularly advantageous from a waste management perspective as it is readily decomposed to form H_2O and O_2 , so

presenting less of a downstream secondary waste challenge than the waste from MEDOC and CORD, e.g. Ce/Mn ion recovery.

There is a broad literature base to support the reaction of bulk UO_2 and H_2O_2 in aqueous media proceeding via the following (electrochemically coupled) reaction scheme [17,18,20-29]:

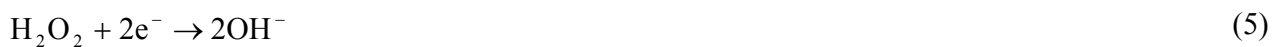
Peroxide decomposition and generation of U(IV)-U(V) sites on UO_2



Anodic reaction

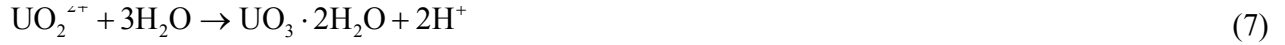


Cathodic reactions



A net hydrogen peroxide reduction reaction occurs via Eq. 1 and 2, facilitated by the creation of U(IV)-U(V) donor-acceptor sites on the UO_2 surface. The balance of electrons for this reduction may be provided by the oxidation of hydrogen peroxide in Eq. 3, with Eqs. 1 to 3 then in effect describing a chemical-electrochemical disproportionation of H_2O_2 to form O_2 and H_2O . The balance of electrons for Eq. 1 and 2, presented in simplified form in Eq. 5, may also be provided by UO_2 oxidation, Eq. 4, that may ultimately result in UO_2 dissolution. As described by Eq. 4, this dissolution is an anodic electrochemical process, involving several surface oxidation steps attributed to O^{2-} incorporation into the vacancy at the centre of the UO_2 fluorite type unit cell [21]. As well as the net cathodic reduction of H_2O_2 given by Eq. 5, Eq. 4 may also couple with the reduction of oxygen, Eq. 6. This oxygen may be derived from the atmosphere, the radiolysis of water or from the oxidation of hydrogen peroxide, Eq. 3.

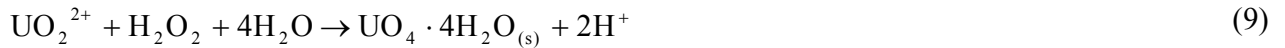
In neutral to alkaline media (pH 7.5) where the solubility of U(VI) is low, low concentrations of $\text{H}_2\text{O}_2 < 100 \mu\text{mol dm}^{-3}$ drive dissolution of the UO_2 surface as UO_2^{2+} via equations 4 & 5 [22,26,30], the UO_2^{2+} subsequently re-precipitating as a patchy schoepite uranyl hydrate phase via the following [30]:



or



At higher concentrations of $\text{H}_2\text{O}_2 > 100 \mu\text{mol dm}^{-3}$ the peroxide both drives UO_2 dissolution and its re-precipitation as the insoluble uranyl tetrahydrate phase, studtite, according to Eq. 9 [22,31,32]:



This studtite layer is observed by Corbel *et al.* [22] to be more even and coherent than the patchy schoepite layer discussed above [30] and so retards the ability of $\text{H}_2\text{O}_2/\text{O}_2$ to oxidise the UO_2 surface by decreasing the area of accessible UO_2 surface presented to solution.

Therefore, in light of the above competing dissolution and precipitation reactions, we wish to understand the effect of H_2O_2 on uranium oxide contaminants on steel in order to better design associated decontamination processes. The removal of entrained uranium necessitates the dissolution of a mixed oxide of U and Fe/Cr/Ni. However, before exploring such materials we wish to study the dissolution of single metal, uranium only oxides as a baseline. To this end thin uranium oxide films have been electrodeposited on to 316L stainless steel planchets to act as a simulated fixed contaminant surface.

Traditional fixed contaminant simulants are produced by either baking thin evaporated uranyl films onto steel planchets [33,34], or by using bulk uranium dioxide powders/pellets [35]. Electrodeposited

uranium oxide provides two benefits over both. First, entrainment of uranium in Fe/Cr/Ni oxide layers is essentially an electrochemical deposition process driven by passivation of the steel surface. Secondly, electrodeposition creates thin uranium oxide layers composed of polymeric U(VI) [36] and/or U(IV) [37], a composition equivalent to that observed in fixed contaminants on process steels [1]. Therefore, in principle electrodeposited uranium oxide more closely simulates the formation of entrained uranium contamination on process steels, both in terms of generation and composition.

Thus, we here describe the nature of the so generated electrodeposited uranium oxide films and, in order to better underpin the design of a simplified peroxide-based decontamination process for uranium contaminated substrates, the effect on the dissolution of those films of peroxide solutions of a wide range of concentrations. Emphasis will be placed on studies at or near neutral pH in order to support development of a secondary waste minimal process wherein liquid waste arisings do not require neutralisation or result in the generation of secondary salt-based wastes. The replacement of traditional acid-based decontamination strategies by such a process will not only obviate corrosion issues associated with the low pH waste but also with the handling of the acid decontamination solution itself.

2. Experimental Section

2.1. Materials

All chemicals were of AnalAR grade or better and supplied by Sigma Aldrich (Gillingham, Dorset, UK) with the exception of 35 wt. % ($\sim 10 \text{ mol dm}^{-3}$) hydrogen peroxide supplied by Fisher Scientific Inc (Loughborough, Leicestershire, UK). In order to avoid significant decomposition of the hydrogen peroxide stock solution, experiments were conducted within two days of opening a freshly received container, the container being stored in a refrigerator during those two days.

All H_2O used was prepared using an Elga Vision 125 instant deionised water cartridge (Marlow, Bucks, UK). This is capable of producing 60 litre/hr of ultra-pure water with a conductivity of less than $1 \mu\text{s/cm}$ (micro siemen per centimeter) to a measured pH of 6.1.

2.2. Preparation of the Electrodeposited Uranium Oxide Films

Uranium oxide was electroplated onto circular 2.54 cm diameter polished 316L stainless steel alpha spectroscopy planchets (Fisher Scientific Ltd, Loughborough, UK) using a standard preparation method developed by the National Nuclear Laboratory (UK), a technique similar to that described by Maya *et al.* [37] and dos Santos *et al.* [36], the principal features of which are as follows.

Electrolyte preparation involved the addition of 0.5 ml of concentrated sulphuric acid to 2 cm^3 of 1 g dm^{-3} uranium (VI) nitrate in 2 % nitric acid (ICP-MS standard). The nitric acid was then evaporated from the resultant solution on a hotplate and the remaining sulphuric acid solution was diluted using 3 cm^3 deionised water before adjusting to pH 2 using 6 cm^3 of dilute sulphuric acid (180 mmol dm^{-3}). The planchets were mounted at the bottom of a disposable polyethylene vial within an electrodeposition cell, an exploded schematic diagram of which is shown in Fig. 1A.

Contact to the planchet, which comprises the cathode of the cell, was made via a stainless steel screw in the bottom section of the electrolysis cell. The electrolysis cell was screwed together as shown in Fig. 1A in order to hold in place both the planchet and the disposable polyethylene vial into which 9 cm^3 of

plating solution has been pipetted. The vial was then capped with a stainless steel plug holding a platinum wire anode.

During electrodeposition, current is delivered by a manifold so that 4 cells can be used at once. For the electrodeposition itself, a potential of 10 V was applied between the cathode and anode of the cell at a current of 1.1-1.2 A for 60 minutes. One minute before the end of the electrolysis, 10 cm³ of 1.45 mol dm⁻³ ammonium hydroxide was added to the cell electrolyte. This was done to stabilise the film by mimicking throughout the cell the local, electrochemically generated basicity at the electrode surface that in part drives film precipitation. At the end of the electrolysis period, the still assembled cell was rinsed with ~5 cm³ of 10 g dm⁻³ ammonium nitrate in 145 mmol dm⁻³ ammonium hydroxide solution. The cell was then disassembled and the planchet washed with deionised water and ethanol before heat treatment on a hot plate at 100 °C for 10 minutes.

2.3. Characterisation of Electroplated Uranium Oxide Films

Electrodeposited uranium oxide films prepared on stainless steel planchets as described in section 2.2 were characterised using a combination of Scanning Electron Microscopy (SEM)/Energy Dispersive X-ray Analysis (EDX), X-ray Diffraction (XRD) and Raman spectroscopy.

SEM images were obtained using a Quanta 200, field emission gun, environmental scanning electron microscope (FEI Ltd, Cambridge, UK). EDX spectra were generated by a combined INCA X-Act series detector (Oxford Instruments, Abingdon, Oxfordshire, UK).

Reflectance Raman spectroscopy was carried out using an InVia Raman Microscope with a 785 nm laser (Renishaw PLC, Wotton-Under-Edge, Gloucestershire, UK). Prior to sample analysis, the detector was calibrated using a pure silicone standard and peak position ($520 \pm 1 \text{ cm}^{-1}$), resolution ($< 5 \text{ cm}^{-1}$) and intensity ($> 30,000$ counts) were checked. Typically, sample analysis involved the recording of 3 spectra from 100 cm^{-1} to 2000 cm^{-1} , 20 seconds acquisition time. Optimal laser power was set to 1% of the maximum laser value ($\sim 1.5 \text{ mW}$) in order to avoid transformation of any UO₂ species to U₃O₈ by laser driven oxidation in air, as reported by Pointurier *et al.* [38].

XRD analysis of the electrodeposited uranium oxide film was conducted using a X'pert XRD system (PANalytical B.V, Almelo, The Netherlands) with CuK (alpha) X-rays at a wavelength of 1.540560Å. Measurements of 2θ were made from 5.01° to 74.97°, with a step width of 0.02° per measurement.

2.4. Hydrogen Peroxide Driven Uranium Oxide Dissolution Studies

Electrodeposited uranium oxide dissolution in hydrogen peroxide solutions of a range of concentrations was monitored *in situ* by open circuit potentiometry using a Pine Instruments AFCBP1 Bipotentiostat (Pine Instrument Company, Grove City, California, USA). For use as a working electrode, uranium oxide-coated stainless steel planchets were placed in a polytetrafluoroethylene (PTFE) electrode holder, see Fig. 1B, so that only the uranium oxide plated face was exposed to solution. Potentials were recorded as a function of planchet immersion time versus a commercial saturated calomel reference electrode (SCE) type CR5 (ThermoRussel, Auchtermuchty, Fife, Scotland).

The working electrode was immersed in 200 ml deionised water to which H₂O₂ aliquots, drawn from a stock solution of 35 wt. %, were added after an immersion period of not more than two minutes. The open circuit potential was recorded chronopotentiometrically for a period of one hour after electrode immersion and the solution was sparged with air throughout the recording period. After completion of each chronopotentiometric run, the planchets were washed with deionised water and left to dry in air. Initially liquid scintillation counting of the experimental solution was attempted. However, peroxide interference with the scintillator (via molecular oxygen quenching) masked any underlying alpha count changes. Instead, absolute alpha count measurements of the sample planchet were taken before and after immersion using a Harwell Instruments Ltd. 956012-1 alpha drawer and BC100 portable counter (Didcot, Oxfordshire, UK), in order to determine any loss of the uranium oxide from the planchet surface. Measurements were taken by a National Nuclear Laboratory standard method with a demonstrable preparation accuracy of 5%. Background counts were taken overnight before any sample counting and calibration was carried out on use by counting a sealed Am-241 source for 300 seconds. Samples were counted for a long count duration of one hour, limiting counting uncertainty to 0.5 to

0.6% (+/- 0.1 Bq). However, a Post-experiment SEM imaging and EDX analysis was conducted as above in order to determine any changes in surface morphology/composition. EDX spectra were taken at a large scanned area size (1.5 mm²) and constant beam energy (30 kV). By comparing the integrated peak area of the underlying steel signal, in particular the peak area of the Fe peak at 6.4 keV over a large sample area to minimise morphology effects, semi-quantitative comparisons can be made between samples as to the overall uranium oxide film thicknesses (see section 3.2.).

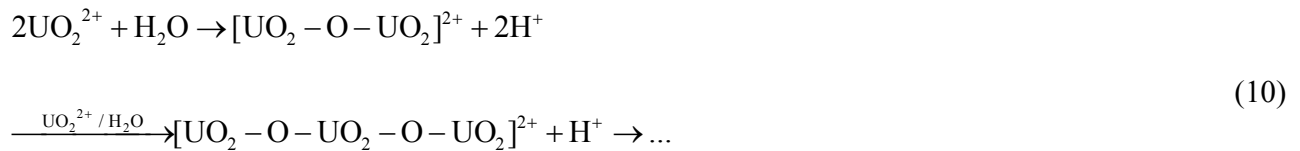
3. Results and Discussion

3.1. Characterisation of Electroplated Uranium Oxide Films

Before studying the effect of hydrogen peroxide on electrodeposited uranium oxide, it is necessary to first characterise the as-prepared films. While the generation of thin uranium oxide films by electrodeposition for isotopic and quantitative analysis of uranium solutions is a widely used technique [39-42], there have been few studies focusing on the composition of the generated films themselves and exact composition varies depending on experimental conditions.

Maya *et al.* [37] have reported the electroplating of thin uranium oxide films on Ni planchets. XPS analysis of these thin films showed that they were pure UO_2 . However, pre and post-deposition microgravimetric studies showed Maya's films to contain 71 wt. % uranium as opposed to an expected uranium content of 88.1 wt. %. The authors attributed this discrepancy to the electrodeposited film being at least in part composed of a hydrated oxide, the existence of which has also been previously suggested by Hufford and Scott [43].

dos Santos *et al.* [36] have studied uranium oxide films electrodeposited onto stainless steel planchets by a method closely related to that described in this work. Using a combination of IR and Raman spectroscopies, and thermogravimetric and XRD analysis they were able to determine that the electrodeposition of uranium oxides from ammonium chloride electrolytes results in the formation of a hydrate of uranium (VI) oxide that is comprised of a polymeric chain compound containing oxygen bridges and is structurally akin to a hydrate of UO_3 :



dos Santos *et al.* also suggest that at high concentrations of ammonium chloride, NH_3 may replace some of the water within the polymeric hydrate structure. The electrodeposited layers are then likely to

be a combination of polymeric structures with a monomeric formula of $\text{UO}_2(\text{OH})_2 \cdot x\text{NH}_3 \cdot y\text{H}_2\text{O}$ and/or $\text{UO}_2(\text{OH})_{2-x} \cdot (\text{ONH}_4)_x \cdot y\text{H}_2\text{O}$ [36]. In order to characterise our electrodeposited uranium oxide films, created as described in section 2, and to compare them with those produced by dos Santos *et al.* [36] and Maya *et al.* [37], a combination of SEM/EDX, XRD and Raman spectroscopy was used to interrogate as-deposited NH_4OH rinsed uranium oxide before and after further exposure to a pH 6.1 deionised water leach.

SEM images of an pre-leach electroplated uranium oxide ‘control’ planchet and a post-leach planchet are shown in Fig. 2A and 2B, respectively. These show that as-prepared uranium oxide films are comprised of three layers: A cracked and patchy seemingly amorphous top layer, perforated with numerous holes through which lower layers can be seen, Fig. 2A; a second, middle layer that appears to be comprised of crystalline particle agglomerates; and a smooth cracked base layer. Fig. 2B also shows the original striated stainless steel surface through breaks in the uranium oxide base layer (steel composition confirmed by EDX analysis, not shown). Comparison of Figs. 2A and 2B also shows the effect of leaching the films in H_2O . Two hours exposure to pH 6.1 H_2O completely removes the top patchy layer and a large proportion of the middle layer. This suggests that both of these upper layers are soluble in aqueous media, the top layer highly so.

Fig. 3 and Fig. 4 show reflective micro Raman spectra of the three identified layers of Fig. 2 and the XRD analysis of the as-electroplated triplex film of Fig. 2A, respectively.

Considering first the Raman analysis of Fig. 3, Fig. 3A shows the spectrum of the surface/near surface of the cracked base layer (lowest layer of those seen in Fig. 2). Absorbance bands are observed at $\sim 764 \text{ cm}^{-1}$ and $\sim 838 \text{ cm}^{-1}$. Comparison of these bands with Raman bands of common uranium oxide/hydroxide/nitrate compounds reported in the literature [31,36,38,44-48], reveals that the Raman spectrum of the cracked base layer is consistent with it being at least in part comprised of polymeric hydrated UO_2^{2+} , as suggested by dos Santos *et al.* [36], main bands at ~ 740 and $\sim 822 \text{ cm}^{-1}$. In their analysis dos Santos *et al.* also indicate that this polymeric hydrated UO_2^{2+} is structurally akin to UO_3

(*vide supra*), a conclusion that is supported by the main bands of orthombic γ - UO_3 being observed at 768 and 845 cm^{-1} .

Comparison of the Raman spectrum of the cracked base layer surface in Fig. 3A with the spectra of the surface/near surface of the particulate morphology middle layer shown in Fig. 3B and patchy top layer shown in Fig. 3C, reveals the retention of the above analysed bands at 838 cm^{-1} and 764 cm^{-1} and the appearance of a new broad band with a peak value at $\sim 660 \text{ cm}^{-1}$, whose relative intensity with respect to the bands at 838 and 764 cm^{-1} increases from Fig. 3B to 3C. A broad, intense Raman band at $\sim 600 \text{ cm}^{-1}$ is indicative of uranyl nitrate, $\text{UO}_2(\text{NO}_3)_2$. However, this band has been seen to shift to $\sim 630 \text{ cm}^{-1}$ upon heating to 100°C [44], a temperature typical of the heat treatment used in the preparation of the samples used in Fig. 3. We therefore associate our observed band at $\sim 660 \text{ cm}^{-1}$ with this heat shifted feature, Palacios and Taylor [44] having attributed this band to an O_2NO asymmetric bending vibration. However, the lack of other features associated with uranyl nitrates suggests that the surfaces/near surfaces of both the middle particulate and upper patchy layer are composed of the same polymeric structure as the base layer, albeit with increasing levels of nitration, nitrate being derived from the post-electrodeposition rinse with $\text{NH}_4\text{OH}/\text{NH}_4\text{NO}_3$.

Turning now to the XRD results of Fig. 4, there is a weak intensity pattern for UO_2 , suggesting that a significant portion of the electrodeposited material is uranium dioxide. Hyper-stoichiometric uranium phases such as UO_{2+x} or higher oxides such as U_4O_9 or U_3O_7 may also be present in the electrodeposit [49]; however the weak signal intensity makes the unambiguous identification of phases such as the latter two difficult. The confirmation or elimination of the presence of non-stoichiometric UO_{2+x} is similarly impeded by signal weakness and complicated by it only being detected by XRD at levels of hyper-stoichiometry high enough to induce distortion of the U sub-lattice, specifically at $x > 0.15$ where transition from the cubic fluorite to tetragonal structure begins [49]. Additionally, given the similarity of its XRD signal to that of UO_2 , the presence of UO_{2+x} at $x < 0.15$ cannot be discounted and, indeed, would be expected given the mode of preparation and solution conditions.

Importantly there are no peaks observed for the higher oxides of U_3O_8 or UO_3 . This corroborates the findings of Maya *et al.* [37] described above, which identify a similarly prepared electrodeposited uranium oxide film on nickel as UO_2 . However, the lack of any characteristic UO_2 or UO_{2+x} Raman bands in Fig. 3, particularly the absence of the Fluorite associated band at 445 cm^{-1} , suggests that the surface/near surface of the film has negligible UO_2 character. Thus, the electrodeposited simulated contaminant may be considered to be composed of a bulk tetravalent UO_2/UO_{2+x} phase, in agreement with Maya, with a surface predominantly comprised of soluble, polymeric hydrated UO_2^{2+} (hydrate of U(VI) oxide) layers, as suggested by dos Santos [36]. Having characterised the contaminant simulant we now describe the dissolution of this material in the presence of H_2O_2 concentrations from $100\text{ }\mu\text{mol dm}^{-3}$ to 1 mol dm^{-3} .

3.2. Exposure of Electrodeposited Uranium Oxide Films to Hydrogen Peroxide Solutions

3.2.1. Alpha Counting, SEM and EDX Measurements

Table 1 and Fig. 5 show the results of *ex situ* alpha counting measurements and SEM images of electrodeposited uranium oxide-plated stainless steel planchets before and after immersion in pH 6.1 deionised water and hydrogen peroxide solutions of concentrations $100\text{ }\mu\text{mol dm}^{-3}$ to 1 mol dm^{-3} .

Considering first the alpha counting results of Table 1. The post-immersion decreases in alpha count can be attributed to either or both of the following: (i) the electrodeposited film dissolving from the steel surface, or (ii) formation via redeposition of dissolved film, of a (self) shielding insoluble corrosion product layer over the electrodeposited film. Given the description of the layer structure developed in section 3.1, two mechanisms for the former process (i) can be envisaged: (i-a) A chemical dissolution involving direct dissolution of the polymeric hydrated uranium (VI) oxide surface phase,; and (i-b) an electrochemical dissolution involving peroxide driven oxidative dissolution of the underlying UO_2/UO_{2+x} layer. The latter process (ii), whilst reducing the rate of uranium dissolution from the oxide film, may lead to a counter-intuitive reduction in alpha count by e.g. introducing more water into the

surface structure of the film resulting in both a lower density of α -emitting uranium per unit volume of surface layer and thus greater self-shielding of emissions from the underlying layer.

Exposure of the electrodeposited film to $100 \mu\text{mol dm}^{-3} \text{H}_2\text{O}_2$ for one hour shows the largest percentage decrease in alpha radiation, larger than the H_2O control and the next highest concentration of H_2O_2 used, 1 mmol dm^{-3} . Comparison of the SEM image of the surface exposed to $100 \mu\text{mol dm}^{-3} \text{H}_2\text{O}_2$, Fig. 5A, with an unexposed surface, Fig. 2A, shows that the soluble upper polymeric hydrated uranium oxide layers of the triplex film have dissolved in a manner similar to that observed for the sample leached for two hours in deionised water, Fig. 2B. However, the base layer of the triplex structure does not show the cracked pattern previously exhibited by this layer in Fig. 2B. Instead striations that match those on the underlying stainless steel disk are apparent. This suggests that the $\text{UO}_2/\text{UO}_{2+x}$ base layer of Fig. 5A is thin in comparison to the analogous layer observed after leaching with H_2O in Fig. 2B, suggesting in turn that some partial dissolution of the H_2O_2 treated $\text{UO}_2/\text{UO}_{2+x}$ layer in Fig. 5A has occurred. In order to obtain a semi-quantitative comparison of film thickness between the H_2O control of Fig. 2B and the $100 \mu\text{mol dm}^{-3} \text{H}_2\text{O}_2$ leached sample in Fig. 5A, EDX measurements were taken at a constant energy and over a large sample area. The overlaid intensities of a 'blank' as-electrodeposited oxide coated planchet (Fig. 2A), a planchet exposed to deionised water only (Fig. 2B) and planchets exposed to $100 \mu\text{mol dm}^{-3} \text{H}_2\text{O}_2$ (Fig. 5A), $10 \text{ mmol dm}^{-3} \text{H}_2\text{O}_2$ (Fig. 5C) and $1 \text{ mol dm}^{-3} \text{H}_2\text{O}_2$ (Fig. 5E) are shown in Fig. 6A.

By comparing the integrated peak area of the underlying steel signal, in particular the Fe peak at 6.4 keV, the reciprocal of the integrated peak area may be considered to be indicative of the uranium oxide layer thickness: The larger the reciprocal integrated peak area, the thicker the layer. Fig. 6B therefore shows a histogram of reciprocal peak areas as a function of the experimental conditions to which the sample has been subjected. In this figure, the reciprocal areas have been normalised to that recorded from the 'blank' as-electrodeposited mixed uranium oxide plated planchet (Fig. 2A), untreated by either a pH 6.1 water leach or H_2O_2 leach.

In Fig. 6B, the reciprocal peak area is largest for the 'blank' untreated film, indicating that this is thickest in comparison to all H₂O/H₂O₂ leached films. Leaching in deionised H₂O for 2 hours significantly decreases the reciprocal peak area and thus, by implication, the thickness of the electrodeposited oxide film. This is in agreement with the SEM image of Fig. 2B, which shows that compared to untreated samples (Fig. 2A) the upper polymeric hydrated uranium oxide layers have been dissolved. Fig. 6B also shows that exposure to 100 μmol dm⁻³ H₂O₂ results in an even lower reciprocal EDX peak area and thus a thinner uranium oxide film compared to the as-prepared 'blank' film and film leached for two hours in H₂O. This is in agreement with the observation of putative thinning of the UO₂/UO_{2+x} base layer in the SEM image of Fig. 5A and the observed greater reduction in alpha count shown in Table 1, 14.3 % for the 100 μmol dm⁻³ H₂O₂ leech compared to 7.6% for the deionised water leach.

Thus, the combined alpha counting and SEM/EDX studies of Fig. 5A and Fig. 6 show that comparatively rapid dissolution of the uranium dioxide film bulk appears to be occurring at 100 μmol dm⁻³ H₂O₂. Importantly no corrosion product layer formation is observed in Fig. 5A, further underpinning the conclusion that the reduction in alpha radiation count in Table 1 can be assumed to be as a direct result of uninhibited dissolution of the polymeric uranium oxide/uranium dioxide film from the stainless steel surface. This is in agreement with previous ICP-MS/Rutherford backscattering spectrometry (RBS) studies of H₂O₂ driven dissolution of UO₂ fuel pellets by Corbel *et al.* [22]. They have shown that at a peroxide concentration of 50 μmol dm⁻³, formation of any corrosion product layer contemporaneously with UO₂ dissolution is slow (~5 hours before any change in the rate of UO₂ dissolution is observed) and any corrosion product layer formed is thin (~100 nm over 112 hours).

Returning to Table 1, immersion of the uranium oxide film in a H₂O₂ solution with a concentration of 1 mmol dm⁻³ results in a smaller count reduction compared to the result obtained at 100 μmol dm⁻³. This smaller reduction in alpha count compared to 100 μmol dm⁻³ H₂O₂ is also observed when using H₂O₂ concentrations of 10 mmol dm⁻³ and 100 mmol dm⁻³. EDX derived film thickness measurements of the 10 mmol dm⁻³ H₂O₂ leached film, Fig. 6B, indicate that the film is of a similar thickness to an as-

prepared electrodeposited film sample. This suggests that dissolution of the polymeric U(VI)/UO₂/UO_{2+x} film is inhibited at peroxide concentrations of 1 mol dm⁻³ and potentially as low as just above 100 μmol dm⁻³. This inhibition is possibly a result of the formation of an insoluble corrosion product layer. Examination of the coincident SEM images, Figs. 5B-5D, reveals a number of changes in surface morphology. Again the upper layers of the polymeric uranium (VI) oxide triplex structure have been fully dissolved. However, the base UO₂/UO_{2+x} layer now has a new lobular surface structure that differs markedly from any of the layer morphologies described above. SEM images of common uranium minerals reported in the literature [22,28,30,50-56] show that the commonly expected UO₂/UO_{2+x} corrosion products of schoepite and studtite are typically fine-grained, sphere-like crystallites and acicular crystals respectively. However, studtite particles or aggregates with a similar lobular morphology to those seen in Figs. 5B-5D have been observed by Douglas *et al.* [55], who have formed studtite powders/aggregates by treatment of a metaschoepite powder with 4 mol dm⁻³ H₂O₂ at pH 5.5 for 6 days. The lack of the typical acicular crystal morphology described by other authors [22,51] is reported by Douglas to be due to both the rapid synthesis of studtite by a high concentration of added H₂O₂ and relatively short ageing time [55]. In order to unequivocally determine the composition of the lobular corrosion product layer described above, Raman spectroscopy measurements was performed on the 100 mol dm⁻³ sample shown in Figure 5D. The results of this analysis are shown in Figure 7.

Figure 7 shows two strong absorbance bands at ~820 and ~864 cm⁻¹ respectively. Literature sources indicate that these bands are associated with the symmetric uranyl stretch ($\nu_1(\text{O}=\text{U}=\text{O})$) and the peroxo ligand stretch ($\nu_2(\text{O}-\text{O})$) of studtite (UO₄·4H₂O) [44,57], confirming that the lobular layer is indeed a studtite corrosion product layer – said layer forming over our electrodeposited uranium oxide films at bulk solution peroxide concentrations down to at least 10⁻³ mol dm⁻³ and possibly as low as just above 10⁻⁴ mol dm⁻³. The latter value is consistent with the work of Clarens *et al.* who report studtite precipitation on UO₂ surfaces at bulk hydrogen peroxide concentrations between 10⁻⁵ and 10⁻⁴ mol dm⁻³ [32,58]. From experiments conducted at pH <4, the solubility constant of studtite has been reported to be 1.3 × 10⁻³ [59].

Returning to the SEM images of electrodeposited uranium oxide film surfaces after exposure to 1, 10 and 100 mmol dm⁻³ H₂O₂, Figs. 5B-5D respectively, Fig. 5D shows that at a H₂O₂ concentration of 100 mmol dm⁻³ the studtite layer is thicker and the lobes are more branched in their morphology compared to 1 mmol dm⁻³ H₂O₂, suggesting the continued growth of the studtite layer over this H₂O₂ concentration regime. This is again in agreement with previous work by Corbel *et al.* [22]. They report that at a [H₂O₂] ≥ 1 mmol dm⁻³ both dissolution and studtite formation occur, the rate of dissolution being low and constant with increasing H₂O₂ concentrations above 1 mmol dm⁻³ whilst the studtite layer thickness increases with both [H₂O₂] and leach time in the same concentration regime.

The concurrent net alpha count changes reported in Table 1 can thus be explained as being functions of both film dissolution and the formation of the self-shielding studtite layer. As described above, dissolution dominates at a [H₂O₂] < 1 mmol dm⁻³ and can now be seen to contribute to the net alpha count reduction at [H₂O₂] ≥ 1 mmol dm⁻³ - albeit at a reduced rate compared to that which obtains at [H₂O₂] ≤ 100 μmol dm⁻³ due to the net dissolution blocking effect of the studtite layer. Given Corbel's ICP-MS/RBS-based observations that the rate of dissolution is constant with increasing [H₂O₂] ≥ 1 mmol dm⁻³, the slight increase in alpha count reduction as [H₂O₂] increases above 1 mmol dm⁻³ is most likely due to a thickening in the studtite layer. This thickening can be observed in the SEM images of Figs. 5B-5D, while the slightly enhanced self-shielding properties of the studtite layer compared to the parent electrodeposited UO₂/UO_{2+x} layer can be attributed to greater water entrainment in the former and thus lower volumetric density of α-emitting sites.

Let us now consider the electrodeposited film surface after exposure to 1 mol dm⁻³ H₂O₂, Fig. 5E, a significantly different morphology to surfaces exposed to lower H₂O₂ concentrations is observed. The lobular studtite structure has begun to show the initial stages of acicular crystal growth on its surface, providing studtite clusters even more similar in size and morphology to those formed by Douglas *et al.* [55]. However, of perhaps greater significance is that the distinctive cracked pattern of the underlying UO₂/UO_{2+x} base layer is not visible, unlike samples exposed to lower H₂O₂ concentrations, Fig. 5B-5D. Instead Fig. 5E shows a striated patterning similar to that observed at a H₂O₂ concentration of 100 μmol

dm^{-3} , Fig. 5A, suggesting that the $\text{UO}_2/\text{UO}_{2+x}$ base layer is again relatively thin and that, as per the $100 \mu\text{mol dm}^{-3}$ treated sample, this is as a result of peroxide-induced dissolution. Support for this putative peroxide-induced thinning of the electrodeposited oxide film is provided by: (1) the alpha counting measurements of Table 1, where at H_2O_2 concentrations $\geq 1 \text{ mol dm}^{-3}$ the alpha count decrease is greater than that observed at $[\text{H}_2\text{O}_2] < 1 \text{ mol dm}^{-3}$ and (2) the EDX measurements of Fig. 6B, from which the reciprocal peak area recorded from the film in $1 \text{ mol dm}^{-3} \text{ H}_2\text{O}_2$ is consistent with the film being thinner than that measured in $10 \text{ mmol dm}^{-3} \text{ H}_2\text{O}_2$. This indicates that previous suggestions that the rate of dissolution at $[\text{H}_2\text{O}_2] \geq 1 \text{ mmol dm}^{-3}$ is relatively constant with increasing $[\text{H}_2\text{O}_2]$ are an oversimplification and that additional re-dissolution of the uranium film or studtite layer may be occurring at $[\text{H}_2\text{O}_2] > 100 \text{ mmol dm}^{-3}$.

3.2.2. Open Circuit Potential Measurements

Having described the physical changes in the electrodeposited polymeric $\text{U(VI)}/\text{UO}_2/\text{UO}_{2+x}$ film with increasing H_2O_2 concentration we now relate this to the *in situ* oxidative stress on the film as quantified by its electrochemical behaviour. Open circuit potential measurements of the electrodeposited uranium film samples exposed to varying hydrogen peroxide concentrations imaged in Figs. 5 and 6 are shown in Fig. 8.

Fig. 8 reveals that, upon immersion of the electrodeposited layers in $100 \mu\text{mol dm}^{-3}$ peroxide, there is a 34 mV increase in the recorded potential from 0.197 to 0.231 V over the one hour period of the experiment. At H_2O_2 concentrations of 1 mmol dm^{-3} and above this increase is greater, the potential in all cases reaching a steady state value of $\sim 0.31 \text{ V}$ after one hour. A summary plot of long immersion time steady state potentials vs. $\log [\text{H}_2\text{O}_2]$ for these samples is shown in the inset to Fig. 8.

Considering the fractured nature of the $\text{UO}_2/\text{UO}_{2+x}$ base layer described in section 3.1, it is possible that the electrochemical behavior of the underlying stainless steel planchet could be controlling the measured open circuit potential. However, potentiometric titration experiments where bare SS316L planchets have been exposed to the same H_2O_2 concentration range, Fig. 9A, show an entirely different

dependence of the measured potential on peroxide concentration compared to that seen in the inset to Fig. 8. This strongly suggests that the measured steady state open circuit potential in Fig. 8 is predominantly controlled by the electrodeposited uranium oxide film. This conclusion is supported by linear sweep voltammetry measurements and SEM images recorded before and after scanning of SS316L planchets in pH 6.1 deionised water, Fig. 9B main and inset. Fig. 9B reveals that in the potential region encompassed by the results of Fig. 8 the steel is passivated and no electrode corrosion is occurring at the steel surface.

In order to understand Fig. 8 in the context of the electrochemistry of uranium dioxide, these results were compared with previously reported studies, recently reviewed and summarised by Shoesmith, of the corrosion behavior of both SIMFUEL and UO_2 electrodes in H_2O_2 free neutral/alkaline solutions, $\text{pH} > 5$ [21]. These indicate that, upon application of potentials more positive than -100 mV to UO_2 SIMFUEL electrodes, oxidation, dissolution and accumulation of corrosion product deposits occurs at the surface, the exact balance between these processes determined by solution conditions. At 200-300 mV the data reviewed by Shoesmith indicates the net formation of schoepite at the uranium oxide surface would be expected in the absence of deliberately added H_2O_2 . However, from the combined SEM/EDX study of section 3.2.1, it would appear that the presence of H_2O_2 in the solution interrupts schoepite formation, resulting in freely dissolving U(VI) species at $[\text{H}_2\text{O}_2] \leq 100 \mu\text{mol dm}^{-3}$ and the formation of an insoluble studtite layer at $[\text{H}_2\text{O}_2] > 100 \mu\text{mol dm}^{-3}$.

Mechanistically this is likely to be due to the formation of uranyl-peroxo complexes [30], which under the conditions employed here are soluble at $[\text{H}_2\text{O}_2] \leq 100 \mu\text{mol dm}^{-3}$ and whose local solubility product is exceeded at the electrodeposited uranium oxide layers surface at $[\text{H}_2\text{O}_2] > 100 \mu\text{mol dm}^{-3}$. Therefore it is reasonable to conclude that the potential of 0.231 V recorded at $[\text{H}_2\text{O}_2] = 100 \mu\text{mol dm}^{-3}$ is primarily associated with peroxide complexed polymeric U(VI)/ $\text{UO}_2/\text{UO}_{2+x}$ dissolution and the more oxidative potential of 0.31 V recorded at $[\text{H}_2\text{O}_2] \geq 1 \text{ mmol dm}^{-3}$ is associated with both initial dissolution and subsequent studtite formation with attendant passivation/inhibition of that dissolution. As the potential does not increase further at peroxide concentrations $\geq 1 \text{ mmol dm}^{-3}$, this may suggest

that dissolution is constant in this concentration regime, an observation in agreement with the results of Corbel *et al.* described previously [22].

Interestingly whilst the steady state potential is independent of $[\text{H}_2\text{O}_2]$ reflecting a constant rate of net dissolution at this value (*vide supra*), the rate at which the potential rises to 0.31 V increases with peroxide concentration, suggesting early control by dissolution that is subsequently inhibited by passivation. This is most clearly seen in trace E of Fig. 8, $[\text{H}_2\text{O}_2] = 1 \text{ mol dm}^{-3}$, where a rapidly rising potential spikes before falling back to 0.31 V, suggesting that dissolution is occurring faster than studtite layer formation for a short time before studtite layer formation inhibits that dissolution and the potential falls back.

Returning to the potentiometric titration of Fig. 9, increasing concentrations of H_2O_2 can be viewed as being equivalent to a linearly increasing externally applied potential to that $\text{UO}_2/\text{UO}_{2+x}$ sample if it were to be used as a working electrode in a conventional electrochemical cell. The alpha count changes reported in Table 1 and the EDX derived indications of film thickness measurements of Fig. 6B may be considered to be reflective of the charge passed during the parallel uranium film dissolution/corrosion product layer growth process during such a pseudo-electrochemical experiment. In turn and via Faraday's law, these changes may also be considered proportional to an average pseudo current passed throughout the sampling period at any one H_2O_2 concentration. This pseudo current, in conjunction with the potentiometric data of Fig. 9 allows us to construct a pseudo-polarisation curve for the electrodeposited uranium film experiments of Table 1 and Figs. 6B, analogous to that shown for steel in Fig. 9B. Such curves are constructed by plotting the percentage decrease in alpha count and/or EDX derived film thickness vs. either the $\log[\text{H}_2\text{O}_2]$ or the open circuit potential obtained at each H_2O_2 concentration employed in the experiment of Fig. 9. Both versions are shown in Fig. 10, which has the general appearance of a linear sweep voltammetry (LSV) experiment on a corroding substrate surface, again analogous to Fig. 9B.

From Fig. 10 regions typical of active, passive and transpassive behaviour can be observed. In light of the above analysis of the processes that dominate at various H_2O_2 concentration regimes, it can be seen

that at $[\text{H}_2\text{O}_2] \leq 100 \text{ } \mu\text{mol dm}^{-3}$, the electrodeposited uranium oxide surface can be considered as being in the active region of the pseudo-LSV and uranium film dissolution proceeds rapidly, unimpeded by any studtite layer. At H_2O_2 concentrations between 1 and 100 mmol dm^{-3} the electrodeposited film can be considered to be in the passivated region of the LSV, said passivation due to the formation of a studtite layer. Accordingly, polymeric $\text{U(VI)/UO}_2/\text{UO}_{2+x}$ dissolution is slow, the gradual increase in the size of the alpha count change here being due to a thickening of the studtite layer as shown by the associated EDX derived film thickness. We believe this is the first electrochemical interpretation of the influence of studtite on the dissolution of a mixed $\text{U(VI)/UO}_2/\text{UO}_{2+x}$ material.

At H_2O_2 concentrations $\geq 1 \text{ mol dm}^{-3}$ the alpha count decrease is greater than that observed at $[\text{H}_2\text{O}_2] < 1 \text{ mol dm}^{-3}$, with the associated EDX measurement indicating a thinner film compared to that measured at $10 \text{ mmol dm}^{-3} \text{ H}_2\text{O}_2$. Comparison with typical LSV experiments on corroding substrate surfaces [60,61] suggests that this corresponds to the system having been driven into a transpassive regime. We believe this to be the first time that such a peroxide-driven passive-transpassive transition has been directly observed on any UO_2 sample.

The origin of the analogous transition in stainless steel systems is the onset of a Cr(III) to Cr(IV) oxidation within the protective passivating film over the steel surface [62]. This results in Cr dissolution from the film with resultant loss of its integrity and so passivating power. As the uranium within the passivating studtite film is already in its +6 oxidation state, the passive-transpassive transition observed in Fig. 10 is unlikely to be associated with an oxidation state change within the film as per the steel system just described. Rather, it would appear that the high peroxide concentrations of $0.1 - 1 \text{ mol dm}^{-3}$ used to access this transition either enable a process that competes with studtite formation or are promoting a non-oxidative dissolution of any formed studtite film. The latter hypothesis is supported by early work by Moskvin [63], who determined from studtite dissolution experiments the formation constants of three uranyl-peroxide complexes, given as UO_2O_2 , $\text{UO}_2(\text{O}_2)_2^{2-}$ and $\text{UO}_2(\text{O}_2)_3^{4-}$. More recent work by Meca *et al.* [64] also reports on the formation constants of 1:1 and 2:1 peroxide-uranium complexes $\text{UO}_2(\text{O}_2)(\text{OH})_2^{2-}$ and $\text{UO}_2(\text{O}_2)_2(\text{OH})_2^{4-}$, deriving $\log\beta^0$ values under pH 12 alkaline

conditions of 28.1 and 36.8 respectively. Using these formation constants, Meca *et al.* calculate speciation diagrams for the uranium-peroxide-water system and find that the 2:1 $\text{UO}_2(\text{O}_2)_2(\text{OH})_2^{4-}$ complex predominates at higher H_2O_2 concentrations of $> \sim 10^{-4} \text{ mol dm}^{-3}$ at pH 12.

This threshold $[\text{H}_2\text{O}_2]$ value for $\text{UO}_2(\text{O}_2)_2(\text{OH})_2^{4-}$ predominance would be expected to increase as pH decreases, and it is informative to consider the solution pH that would be associated with the passive-transpassive transition of Figure 10 if that transition is due to to-solution release of $\text{UO}_2(\text{O}_2)_2(\text{OH})_2^{4-}$ from the studtite passivated electrodeposited films under study here. Thus, using $\log\beta^0$ from Meca *et al.* a predominance diagram has been calculated for the two peroxide-complexes $\text{UO}_2(\text{O}_2)(\text{OH})_2^{2-}$ and $\text{UO}_2(\text{O}_2)_2(\text{OH})_2^{4-}$ as a function of pH and peroxide concentration. This diagram is shown in Fig. 11 with calculations available in the electronic supporting material.

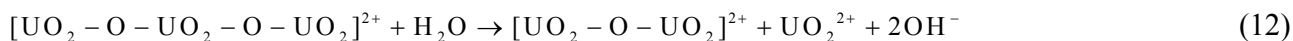
The change from passive to transpassive behaviour of the electrodeposited film under study in Fig. 10 can be seen to occur in a peroxide concentration range of 0.1–1 mol dm^{-3} . At the lower end of this range, 0.1 mol dm^{-3} , Fig. 11 indicates that the $\text{UO}_2(\text{O}_2)(\text{OH})_2^{2-}$ complex is the predominant form of U(VI) in solution at $\text{pH} > 8.6$; at the upper end of this range $[\text{H}_2\text{O}_2] = 1 \text{ mol dm}^{-3}$, then the same complex will dominate solution phase U(VI) behaviour at $\text{pH} > 7.6$. The bulk solution pH at both 0.1 and 1 mol dm^{-3} is measured to be 6.1 – however, this may be locally raised at the film surface as a result of the main routes to the formation from the film of free UO_2^{2+} , the formation of which is evidenced by its following reaction to form studtite at $100 \text{ mmol dm}^{-3} \geq [\text{H}_2\text{O}_2] > 100 \text{ } \mu\text{mol dm}^{-3}$, see Fig. 10. Based on the triplex structure of the film elucidated in section 3.2.1, the two main routes to such free UO_2^{2+} formation would be expected to be:

(i) peroxide-driven oxidative dissolution of the lower layers of the as-electrodeposited film as described by Eq. 11;



where Eq. 11 is the net form of Eqs.4 and 5; and

(ii) dissolution of the film's upper layer, comprised of a hydrated and readily dissolved polymeric uranium (VI) oxide as described by Eq. 12:



From this, it can be seen that both oxidative and non-oxidative UO_2^{2+} generation from the electrodeposited film is accompanied by hydroxide generation with the same uranyl / hydroxide stoichiometries. The reactions of Eqs 11 and 12 are then necessarily accompanied by a local pH increase at the film surface. Given the demonstrable solubility of the upper polymeric uranium (VI) oxide layer of the triplex electrodeposited film (see Fig. 2), the release by the reaction of Eq. 12 of hydroxide ions sufficient to raise the local solution pH from 6.1 to at least 7.6 does not seem unfeasible. Under these conditions, and at 1 mol dm^{-3} of H_2O_2 , Fig. 10 shows that $\text{UO}_2(\text{O}_2)(\text{OH})_2^{2-}$ complex formation may occur and so compete with studtite layer generation – thus reducing the net yield of the latter and resulting in the transition from passive to transpassive behaviour inferred from Fig. 10.

More broadly, the observation of a movement from passive to transpassive behavior with increasing peroxide concentration has implications for the development and application of a simplified, low acidity/near neutral, peroxide based decontamination strategy for U contaminated metal surfaces – specifically, effective surface decontamination of metal substrates may be possible using decontamination agents that contain peroxide concentrations of at least 0.1 mol dm^{-3} and are mildly alkaline, $\text{pH} > 10.6$ roughly that of medicinal milk of magnesia. Such a method would have the significant advantage of being oxidative metal ion free, c.f. CORD, MEDOC etc, with consequent reduced secondary waste requirements. Further, the liquid waste arisings would also require minimal (if any) neutralisation, the replacement of traditional acid-based decontamination processes obviating corrosion issues associated with the handling of both the acid decontaminating solution and its low pH waste.

Finally, the data of Fig. 10 may also have implications for geological disposal. Assuming a near field H_2O_2 concentration of $4 \mu\text{mol dm}^{-3} \text{H}_2\text{O}_2$ [65] and a groundwater pH near neutral, then Fig. 10 suggests that $\text{UO}_2/\text{UO}_{2+x}$ may actively corrode with the resultant species passing into solution and thus be available for environmental release, rather than re-precipitating as schoepite, studtite or related transformation phases. It should be noted that this is a simplification of groundwater conditions and that carbonate would be expected in groundwater / concrete water in repositories, the presence of which has also been shown to enhance net U(VI) dissolution [17,23]. Thus, the effect of carbonated peroxide solution on electrodeposited $\text{UO}_2/\text{UO}_{2+x}$ is currently under study in order to determine its potential for exploitation in decontamination applications as well as its implications for labilising the release of U(VI) species from spent uranium oxide-based nuclear fuel – either in the context of geologic disposal or the COL process (*vide supra*) for spent fuel pellet dissolution.

4. Conclusion

Mixed uranium oxide films have been successfully electrodeposited onto 316L stainless steel planchets – for use as model uranium contaminated surfaces – and the effect of hydrogen peroxide on these films has been studied and determined.

The structure of the film has been found to be predominantly $\text{UO}_2/\text{UO}_{2+x}$ with a surface/near surface phase comprised a polymeric hydrated uranium (VI) oxide akin to a UO_3 hydrate. The dissolution of these deposited films in the presence of deliberately added hydrogen peroxide has been studied using a combination of open circuit potentiometry, alpha counting and SEM/EDX imaging and explained in terms of a corrosion-based description. The results of these analyses have shown that at $[\text{H}_2\text{O}_2] \leq 100 \mu\text{mol dm}^{-3}$ the uranium oxide film is actively corroding with a dissolution rate significantly greater than that observed during the leaching of similar films in pH 6.1 peroxide-free water. This confirms that, at peroxide concentrations of $\sim 4 \mu\text{mol dm}^{-3}$, typical of those expected in the near field of spent nuclear fuel in geologic repository, UO_2 may actively corrode with the resultant species passing into solution and thus be available for environmental release, rather than re-precipitating as schoepite, studtite or related transformation phases.

On the other hand, at H_2O_2 concentrations between 1 mmol dm^{-3} and 0.1 mol dm^{-3} , formation of an insoluble studtite corrosion product layer occurs at the film surface, suggesting that under such conditions $\text{UO}_2/\text{UO}_{2+x}$ may self-protect against corrosion-driven environmental release. At $[\text{H}_2\text{O}_2] > 0.1 \text{ mol dm}^{-3}$ the electrodeposited film exhibits a transpassive response and can dissolve – the first time this change in behaviour has been observed in UO_2 solution peroxide containing systems. We postulate that this transition from passive to transpassive behaviour is due to the formation of soluble uranyl-peroxide complexes under mildly alkaline, high $[\text{H}_2\text{O}_2]$ conditions, a conclusion that has implications for the design of both metal ion oxidant-free, acid minimal decontamination strategies with low secondary waste arisings, and single step processes for spent nuclear fuel dissolution such as the COL process.

Acknowledgements. This work was supported by the Engineering and Physical Sciences Research Council (EPSRC), the Nuclear Decommissioning Authority (NDA) and the National Nuclear Laboratory (NNL) via an Industrial CASE award for RJW.

CB is supported by The Lloyd's Register Foundation (LRF). The Lloyd's Register Foundation helps to protect life and property by supporting engineering-related education, public engagement and the application of research.

References and Notes

- [1] C.J. Dodge, A.J. Francis, J.B. Gillow, G.P. Halada, C. Eng, and C.R. Clayton, *Environ. Sci. Technol.*, 36 (2002) 3504-3511.
- [2] A.J. Francis, C.J. Dodge, J.A. McDonald, and G.P. Halada, *Environ. Sci. Tech.*, 39 (2005) 5015-5021.
- [3] P. Dombovari, P. Kadar, T. Kovacs, J. Somlai, K. Rado, I. Varga, R. Bujak, K. Varga, P. Halmos, J. Borszeki, J. Konya, N.M. Nagy, L. Kover, D. Varga, I. Cserny, J. Toth, L. Fodor, A. Horvath, T. Pinter, and J. Schunk, *Electrochim. Acta*, 52 (2007) 2542-2551.
- [4] E. Liger, L. Charlet, and P. Van Cappellen, *Geochim. Cosmochim. Acta*, 63 (1999) 2939-2955.
- [5] J.P. Caire, F. Laurent, S. Cullie, F. Dalard, J.M. Fulconis, and H. Delagrangé, *J. Appli. Electrochem.*, 33 (2003) 703-708.
- [6] J.P. Caire, S. Cullie, F. Dalard, M. Fulconis, and H. Delagrangé, *J. Appli. Electrochem.*, 33 (2003) 709-715.

- [7] M. Dubourg, Nucl. Eng. Des., 159 (1995) 123-129.
- [8] M. Matheswaran, S. Balaji, S.J. Chung, and I.S. Moon, Catal. Commun., 8 (2007) 1497-1501.
- [9] T. Suwa, N. Kuribayashi, and E. Tachikawa, J. Nucl. Sci. Technol., 23 (1986) 622-632.
- [10] T. Suwa, N. Kuribayashi, and E. Tachikawa, J. Nucl. Sci. Technol., 25 (1988) 574-585.
- [11] D. Bradbury, Review of decontamination technology development 1977-2000, in: British Nuclear Energy Society (Ed.), Water chemistry of nuclear reactor systems 8, Vol. 1. Thomas Telford Ltd, 2001, pp. 173-178.
- [12] I. Inami, Y. Sato, T. Kanasaki, N. Suzuki, A. Fujimori, A. Makihira, H. Wille, and F. Strohmer, Contribution to dose rate reduction for core internals replacement work by full system decontamination, in: British Nuclear Energy Society (Ed.), Water chemistry of nuclear reactor systems 8, Vol. 2. Thomas Telford Ltd, 2001, pp. 444-450.
- [13] H. Wille and H.O. Bertholdt, Nuclear Europe, 8 (1988) 41-42.
- [14] H. Wille and H.O. Bertholdt, The CORD UV concept for decontamination and the application experience, in: British Nuclear Energy Society (Ed.), Water chemistry of nuclear reactor systems 7, Vol. 1. Thomas Telford Ltd, 1996, pp. 317-323.
- [15] H. Wille and H.O. Bertholdt, Lessons learned in full system decontamination by application of the CORD family concept, in: British Nuclear Energy Society (Ed.), Water chemistry of nuclear reactor systems 8, Vol. 1. Thomas Telford Ltd, 2001, pp. 179-184.
- [16] K.W. Kim, G.I. Park, E.H. Lee, K.W. Lee, and K.C. Song, Int. J. Chem. Biol. Eng., 3 (2010) 187-190.
- [17] J.S. Goldik, J.J. Noel, and D.W. Shoesmith, Electrochim. Acta, 51 (2006) 3278-3286.

- [18] S. Sunder, N.H. Miller, and D.W. Shoesmith, *Corros. Sci.*, 46 (2004) 1095-1111.
- [19] C. Soderquist and B. Hanson, *J. Nucl. Mater.*, 396 (2010) 159-162.
- [20] J.S. Goldik, H.W. Nesbitt, J.J. Noel, and D.W. Shoesmith, *Electrochim. Acta*, 49 (2004) 1699-1709.
- [21] D.W. Shoesmith, *J. Nucl. Mater.*, 282 (2000) 1-31.
- [22] C. Corbel, G. Sattonnay, S. Guilbert, F. Garrido, M.F. Barthe, and C. Jegou, *J. Nucl. Mater.*, 348 (2006) 1-17.
- [23] E. Ekeröth and M. Jonsson, *J. Nucl. Mater.*, 322 (2003) 242-248.
- [24] M.M. Hossain, E. Ekeröth, and M. Jonsson, *J. Nucl. Mater.*, 358 (2006) 202-208.
- [25] J.S. Goldik, J.J. Noël, and D.W. Shoesmith, *J. Electroanal. Chem.*, 582 (2005) 241-248.
- [26] O. Roth, M. Jonsson, *Cent. Eur. J. Chem.*, 6 (2008) 1-14.
- [27] P.G. Keech, J.J. Noël, and D.W. Shoesmith, *Electrochim. Acta*, 53 (2008) 5675-5683.
- [28] G. Sattonnay, C. Ardois, C. Corbel, J.F. Lucchini, M.F. Barthe, F. Garrido, and D. Gosset, *J. Nucl. Mater.*, 288 (2001) 11-19.
- [29] R. Pehrmen, M. Amme, O. Roth, E. Ekeröth, and M. Jonsson, *J. Nucl. Mater.*, 397 (2010) 128-131.
- [30] M. Amme, *Radiochim. Acta*, 90 (2002) 399-406.
- [31] M. Amme, B. Renker, B. Schmid, M.P. Feth, H. Bertagnolli, and W. Döbelin, *J. Nucl. Mater.*, 306 (2002) 202-212.

- [32] F. Clarens, J. De Pablo, I. Diez-Perez, I. Casas, J. Gimenez, and M. Rovira, *Environ. Sci. Tech.*, 38 (2004) 6656-6661.
- [33] C.K. McKeown and B.H. Davison, *Health Phys.*, 86 (2004) S113-S115.
- [34] R.L. Demmer, Development of simulated contaminants (SIMCON) and miscellaneous SIMCON scoping tests. OSTI DE94013807, 1994. Idaho National Engineering laboratory, USA
- [35] B.G. Santos, J.J. Noël, and D.W. Shoesmith, *J. Electroanal. Chem.*, 586 (2006) 1-11.
- [36] L.R. dos Santos, M.E. Sbampato, and A.M. dos Santos, *J. Radioanal. Nucl. Chem.*, 261 (2004) 203-209.
- [37] L. Maya, B.D. Gonzalez, M.J. Lance, and D.E. Holcomb, *J. Radioanal. Nucl. Chem.*, 261 (2004) 605-607.
- [38] F. Pointurier and O. Marie, *Spectrochim. Acta. B*, 65 (2010) 797-804.
- [39] J.E. Evans, R.W. Loughheed, R.W. Hoff, E.K. Hulet, and M.S. Coops, *Nucl. Instrum. Methods*, 102 (1972) 389-401.
- [40] A.H.F. Muggleton, *J. Phys. E-Sci. Instrum.*, 12 (1979) 780-807.
- [41] L. Yaffe, *Annu. Rev. Nucl. Sci.*, 12 (1962) 153-188.
- [42] N.A. Talvitie, *Anal. Chem.*, 44 (1972) 280-&.
- [43] D.L. Hufford and B.F. Scott, Techniques for the preparation of thin films of radioactive material. MDDC-1515, 28-30. 1945. United States Atomic Energy Commission.
- [44] M.L. Palacios and S.H. Taylor, *Appl. Spectrosc.*, 54 (2000) 1372-1378.

- [45] S.D. Senanayake, R. Rousseau, D. Colegrave, and H. Idriss, *J. Nucl. Mater.*, 342 (2005) 179-187.
- [46] E.A. Stefaniak, A. Alsech, I.E. Sajó, A. Worobiec, Z. Máthé, S. Török, and R.V. Grieken, *J. Nucl. Mater.*, 381 (2008) 278-283.
- [47] C. Jégou, R. Carabello, S. Peugeot, D. Roudil, L. Desgranges, and M. Magnin, *J. Nucl. Mater.*, 405 (2010) 235-243.
- [48] D. Ofori, P.G. Keech, J.J. Noël, and D.W. Shoesmith, *J. Nucl. Mater.*, 400 (2010) 84-93.
- [49] H. He and D.W. Shoesmith, *Phys. Chem. Chem. Phys.*, 12 (2010) 8108-8117.
- [50] A.G. Sowder, S.B. Clark, and R.A. Fjeld, *Environ. Sci. Tech.*, 33 (1999) 3552-3557.
- [51] M. Deliens and P. Piret, *Am. Mineral.*, 68 (1983) 456-458.
- [52] M.D. Kaminski and M.M. Goldberg, *J. Nucl. Mater.*, 304 (2002) 182-188.
- [53] F. Clarens, J. De Pablo, I. Casas, J. Gimenez, M. Rovira, J. Merino, E. Cera, J. Bruno, J. Quinones, and A. Martinez-Esparza, *J. Nucl. Mater.*, 345 (2005) 225-231.
- [54] J.C. Clayton and S. Aronson, *J. Chem. Eng. Data*, 6 (1961) 43-51.
- [55] M. Douglas, S.B. Clark, J.I. Friese, B.W. Arey, E.C. Buck, and B.D. Hanson, *Environ. Sci. Tech.*, 39 (2005) 4117-4124.
- [56] H.J. Matzke, *J. Nucl. Mater.*, 238 (1996) 58-63.
- [57] S. Bastians, G. Crump, W.P. Griffith, and R. Withnall, *J. Raman Spectrosc.*, 35 (2004) 726-731.
- [58] F. Clarens, J. Gimenez, J. de Pablo, I. Casas, M. Rovira, J. Dies, J. Quinones and A. Martinez-Esparza, *Radiochim. Acta.*, 93 (2005) 533-539.

- [59] K. A. Hughes-Kubatko, K. B. Helean, A. Navrotsky and P. C. Burns, *Science*, 302 (2003) 1191
- [60] G. Carbajal-de la Torre, M.A. Espinosa-Medina, A. Martinez-Villafane, J.G. Gonzalez-Rodriguez, and V.M. Castano, *The Open Corrosion Journal*, 2 (2009) 197-203.
- [61] M. Itagaki, H. Nakazawa, K. Watanabe, and K. Noda, *Corros. Sci.*, 39 (1997) 901-911.
- [62] B. Gwinner, M. Auroy, D. Mas, A. Saint-Jevin and S. Pasquier-Tilliette, *J. Nucl. Mater.*, 428 (2012) 110-116
- [63] A. I. Moskvina, *Radiokhimiya*, 10 (1968) 13
- [64] S. Meca, A. Martinez-Torrents, V. Marti, J. Gimenez, I. Casas and J. de Pablo, *Dalton Trans.*, 40 (2011) 7976-7982
- [65] E. C. Buck, R. S. Wittman, F. N. Skomurski, K. J. Cantrell, B. K. McNamara and C. Z. Soderquist, *Radiolysis Process Modelling Results for Scenarios*, FCRD-UFD-2012-000199, 2-5. 2012. U.S. Department of Energy Separations/Waste Form Campaign.

Tables

Hydrogen Peroxide Concentration	Alpha Count (Bq) Before	Alpha Count (Bq) After	% Alpha Decrease
Control (No addition)	23.8 (+/-1.3)	22.0 (+/-1.2)	7.6
100 $\mu\text{mol dm}^{-3}$	24.5 (+/-1.4)	21.0 (+/-1.2)	14.3
1 mmol dm^{-3}	25.4 (+/-1.4)	23.4 (+/-1.3)	7.9
10 mmol dm^{-3}	25.0 (+/-1.4)	22.9 (+/-1.3)	8.4
100 mmol dm^{-3}	25.1 (+/-1.4)	22.8 (+/-1.3)	9.2
1 mol dm^{-3}	21.9 (+/-1.2)	19.0 (+/-1.1)	13.2

Table 1. Alpha count of electrodeposited uranium oxide-plated stainless steel planchets before and after one hour leach periods in pH 6.1 water (as control) and 100 $\mu\text{mol dm}^{-3}$, 1 mmol dm^{-3} , 10 mmol dm^{-3} , 100 mmol dm^{-3} and 1 mol dm^{-3} solutions of H_2O_2 .

Figure Captions

Fig. 1. Exploded schematics of (A) the electrodeposition cell and (B) the PTFE electrode holder.

Fig. 2. 2000x magnification SEM image of a uranium oxide-coated steel planchet: (A) as-electrodeposited, (B) after exposure to a two hour leach in pH 6.1 deionised water.

Fig. 3. Raman spectra of the three layers of the triplex structure of the untreated electrodeposited uranium oxide film of Fig. 2: (A) the cracked base layer, (B) the crystalline middle layer and (C) the top amorphous layer.

Fig. 4. XRD spectrum of the untreated, electrodeposited uranium oxide-coated stainless steel planchet of Fig. 2a. Peaks associated with UO_2 and 316L steel (γ -austenite) are as marked.

Fig. 5. 2000x magnification SEM images showing the effect of 1 hour exposure to solution of H_2O_2 on electrodeposited uranium oxide-coated steel planchets. Concentration of peroxide used: (A) $100 \mu\text{mol dm}^{-3} \text{H}_2\text{O}_2$ for 1 hour, (B) $1 \text{ mmol dm}^{-3} \text{H}_2\text{O}_2$ for 1 hour, (C) $10 \text{ mmol dm}^{-3} \text{H}_2\text{O}_2$ for 1 hour, (D) $100 \text{ mmol dm}^{-3} \text{H}_2\text{O}_2$ for 1 hour, (E) $1 \text{ mol dm}^{-3} \text{H}_2\text{O}_2$, all in pH 6.1 water sparged with air.

Fig. 6. (A) 30 keV EDX spectra of uranium oxide plated stainless steel planchets exposed to a variety of H_2O_2 concentrations. (B) Histogram of film thickness parameter as a function of the indicated experimental conditions to which samples have been subjected. The film thickness parameter is derived from the reciprocal of the integrated peak area of the Fe 6.4 keV EDX peak, normalised to that of a 'blank' untreated electrodeposited sample, as described in the text.

Fig. 7. Raman spectrum of the lobular corrosion product layer formed by treatment of a electrodeposited uranium oxide-coated stainless steel planchet with $100 \text{ mmol dm}^{-3} \text{H}_2\text{O}_2$ for one hour (Fig. 6d).

Fig. 8. Open circuit potential vs. time traces (main) and $\log[\text{H}_2\text{O}_2]$ vs. steady state potential (inset) for uranium oxide-coated steel planchets, prepared as Fig. 2a, immersed in the following concentration solutions of H_2O_2 in pH 6.1 water sparged with air: (A) $100 \mu\text{mol dm}^{-3}$, (B) 1 mmol dm^{-3} (C) 10 mmol dm^{-3} , (D) 100 mmol dm^{-3} and (E) 1 mol dm^{-3} . $t = 0$ corresponds to the point of immersion.

Fig. 9. (A) Steady state open circuit potential vs. $\log [\text{H}_2\text{O}_2]$ for a SS316L electrode immersed in a range of H_2O_2 solutions in pH 6.1 water. $R^2 = 0.997$. $m = 70$ mV/decade. (B) Polarisation curve of a SS316L electrode immersed in 0.5 mol dm^{-3} Na_2SO_4 adjusted to pH 6.1 (Main) and SEM images taken before and after scanning (Inset).

Fig. 10. Pseudo-current vs. potential pseudo-polarogram, constructed from the data of Table 1 and Figs. 6b and 9 as described in the text, illustrating the effect of the mixed potentials generated by increasing hydrogen peroxide concentrations on the corrosion of an electrodeposited uranium oxide-coated SS316L planchet in pH 6.1 deionised water.

Fig. 11. Calculated predominance diagram of uranyl-peroxide species as a function of pH and H_2O_2 concentration.

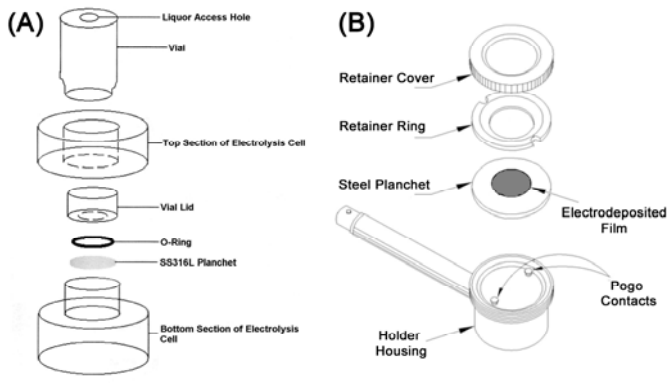


FIGURE 1

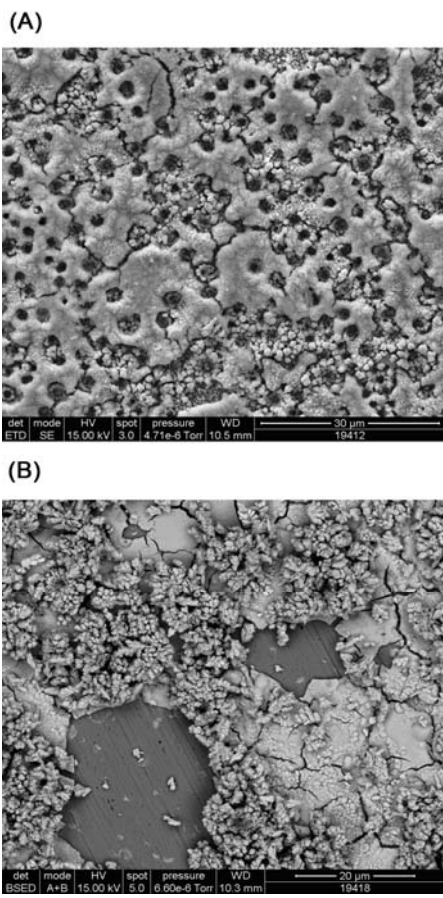


FIGURE 2

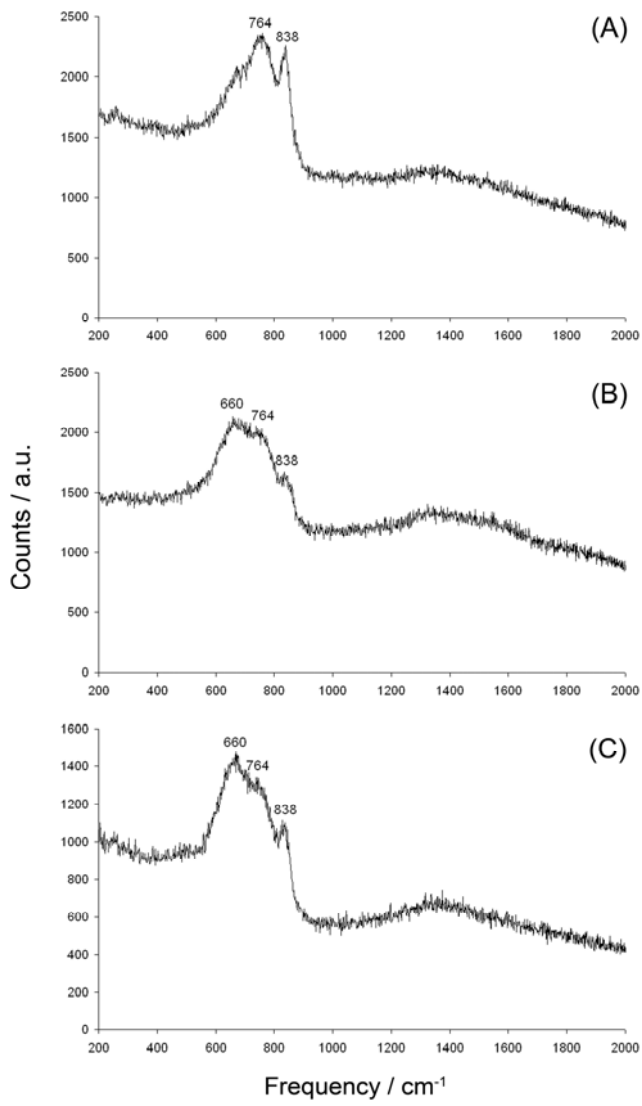


FIGURE 3

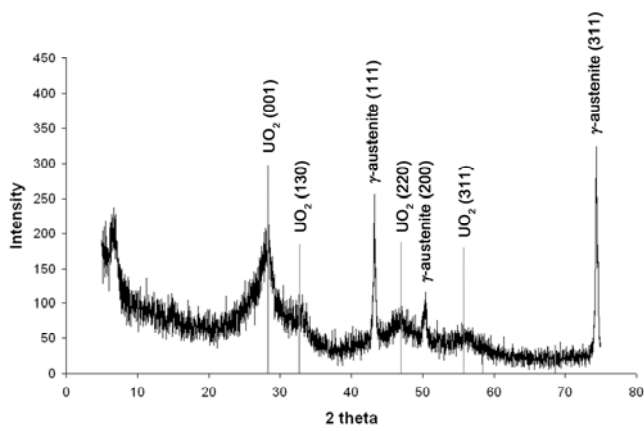


FIGURE 4

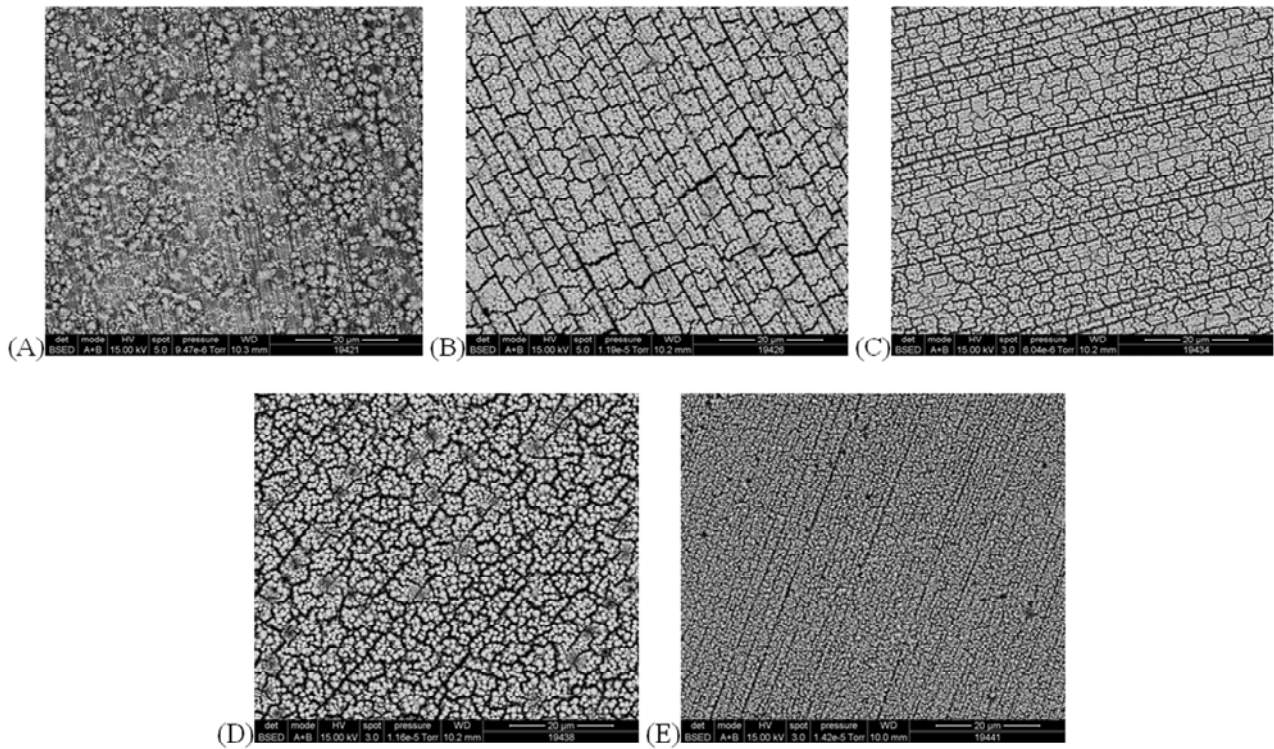


FIGURE 5

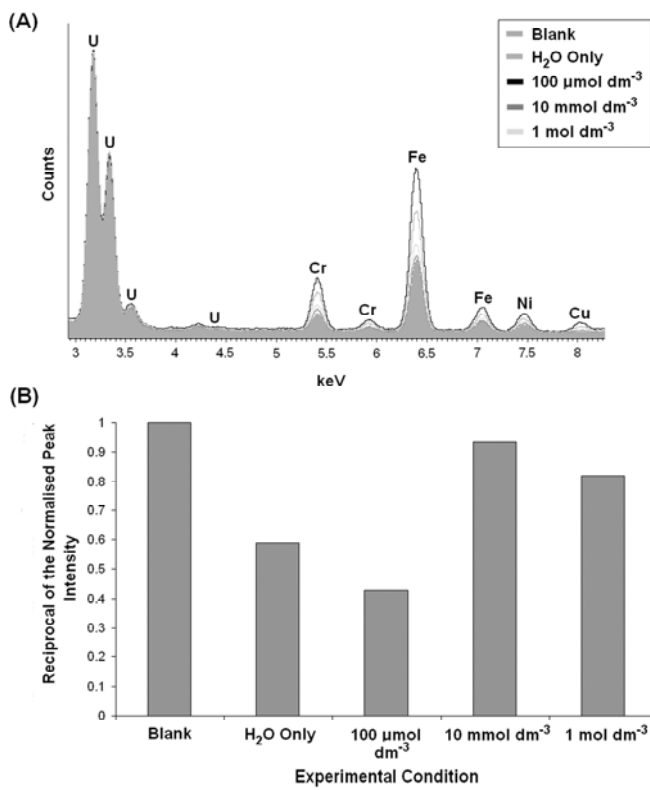


FIGURE 6

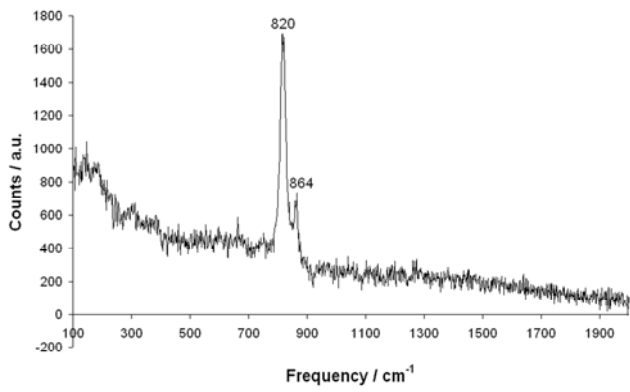


FIGURE 7

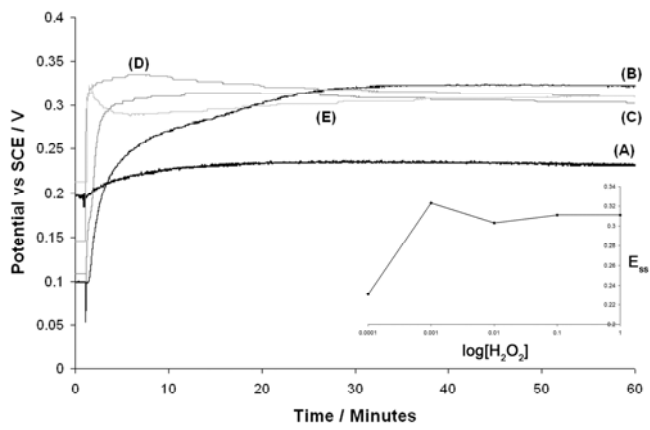


FIGURE 8

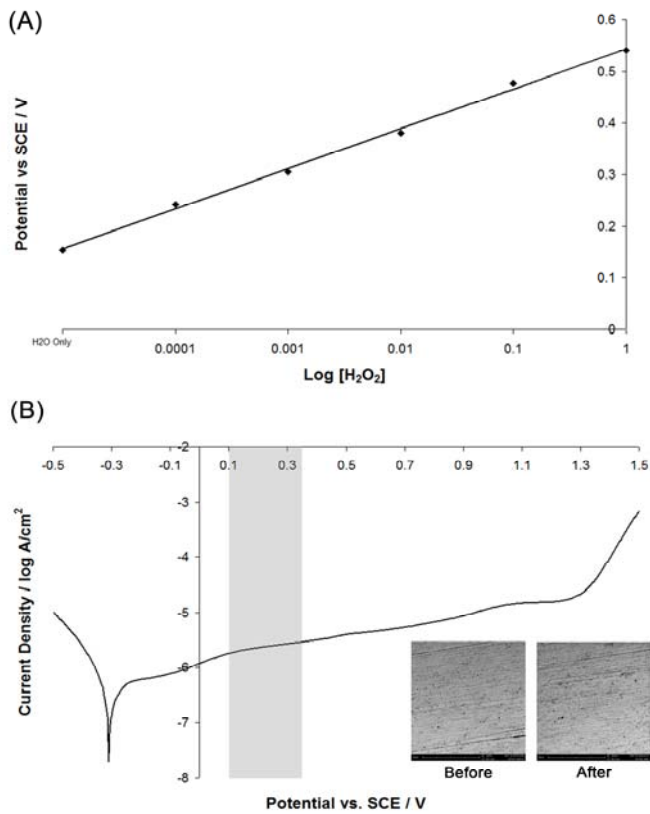


FIGURE 9

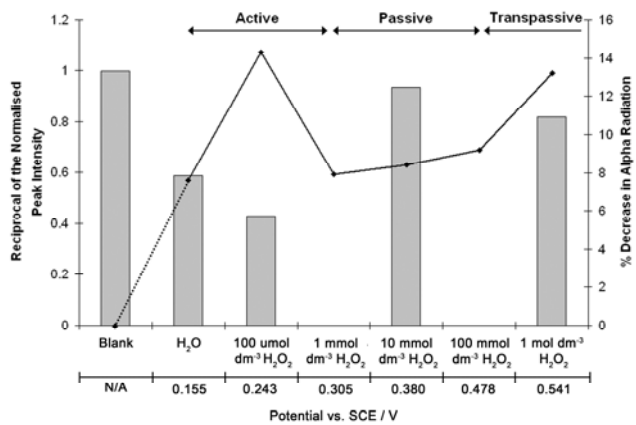


FIGURE 10

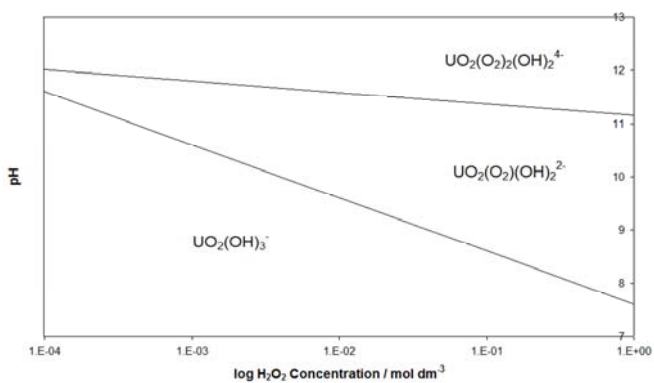


FIGURE 11